Title

Bimetal—Organic Framework Self-Adjusted Synthesis of Support-Free Nonprecious Electrocatalysts for Efficient Oxygen Reduction

Journal

ACS Catalysis, 5(12)

ISSN

2155-5435

Authors

You, Bo

Jiang, Nan

Sheng, Meili

et al.

Publication Date

2015-12-04

DOI

10.1021/acscatal.5b02325

Peer reviewed

Bimetal-Organic Framework Self-Adjusted Synthesis of Support-Free Nonprecious Electrocatalysts for Efficient Oxygen Reduction

Bo You,[†] *Nan Jiang*,[†] *Meili Sheng*,[†] *Walter S. Drisdell*,[‡] *Junko Yano*,[‡,§] *and Yujie Sun*[†*]

[†] Department of Chemistry and Biochemistry, Utah State University, 0300 Old Main Hill, Logan, Utah 84322 (USA)

[‡] Joint Center of Artificial Photosynthesis, Berkeley, CA 94720 (USA)

[§] Physical Biosciences Division, Lawrence Berkeley National Laboratory, Berkeley, CA 94720 (USA).

KEYWORDS. oxygen reduction; electrocatalyst; metal-organic framework; self-adjusted; nonprecious

ABSTRACT

The development of low-cost catalysts with oxygen reduction reaction (ORR) activity superior to that of Pt for fuel cells is highly desirable but remains challenging. Herein, we report a bimetal-organic framework (bi-MOF) self-adjusted synthesis of support-free porous Co-N-C nanopolyhedron electrocatalysts by pyrolysis of Zn/Co bi-MOF without any post-treatments. The presence of initial Zn forms a spatial isolation of Co which suppresses its sintering during pyrolysis and the Zn evaporation also promotes the surface area of the resultant catalysts. The composition, morphology, and hence ORR activity of Co-N-C could be tuned by the Zn/Co ratio. The optimal Co-N-C exhibited remarkable ORR activity with a half-wave potential of 0.871 V vs RHE (30 mV more positive than that of commercial 20 wt% Pt/C) and a kinetic current density of 39.3 mA cm^{-2} at 0.80 V vs RHE (3.1 times that of Pt/C) in 0.1 M KOH, plus excellent stability and methanol tolerance. It also demonstrated comparable ORR activity and much higher stability than those of Pt/C in acidic and neutral electrolytes. Various characterization techniques including X-ray absorption spectroscopy revealed that the superior activity and strong stability of Co-N-C originated from the intense

interaction between Co and N, high content of ORR active pyridinic and pyrrolic N as well as large specific surface area.

Electrochemical oxygen reduction is a crucial and limiting process for several emerging renewable energy technologies that operate in acidic (proton exchange membrane fuel cells), basic (alkaline fuel cells or chlor-alkali electrolyzers), or neutral (microbial fuel cells) electrolytes.[1−2345678] Although Pt-based materials have proven to be excellent ORR catalysts, the prohibitive cost, scarce reserve, poor durability, and methanol crossover significantly prohibit their large-scale application.[1−910111213] Consequently, great efforts have been devoted to developing nonprecious alternatives such as earth-abundant metal alloys,[10] transition metal oxides,[2] and metal-free heteroatom-doped carbons,[14−1516171819202122] among which, transition metal-nitrogen-carbon (M-N-C) composites have attracted increasing interest owing to their low-cost and comparable catalytic activity.[9,23−2425262728293031323334 35] However, most reported M-N-C electrocatalysts still require higher ORR overpotential than that of Pt in alkaline media,[26−28] partially due to the nonuniform and insufficient exposure of catalytic active sites resulting from the lack of accurate control of the catalyst composition and/or structure. In addition, the usually tedious post-treatment procedures, such as longstanding hot acid leaching and/or iterative high temperature annealing (Tables S1 and S2 in Supporting Information), significantly increase their cost of scalable production.[9,23−36] Hence, we seek to develop earth-abundant catalysts via low-cost preparation methods for various energy applications.[37,38]

Resulting from the unique features of high specific surface area, controllable pore texture, and diverse composition, metal-organic frameworks (MOFs) offer an opportunity to obtain competent ORR electrocatalysts after carbonization.[39−40414243444546] However, due to the limited thermal stability, directly carbonized MOF usually suffer from low specific surface area and thus mediocre catalytic activity.[41] Accordingly, high surface area supports or exotic additives are typically needed, which complicate the synthetic procedures. In fact, most of these composites still show inferior ORR activity compared to Pt.[39−44] Therefore, it is highly desirable to explore a simple and scalable method to achieve self-supported MOF-derived nonprecious electrocatalysts with ORR activity better than that of Pt.

Herein, we report a facile and novel Zn and Co bi-MOF self-adjusted route to produce self-supported Co-N-C nanopolyhedrons as superior ORR electrocatalysts by direct pyrolysis of Zn_xCo_{1-}

$_x(MeIM)_2$ frameworks (MeIM = 2-methylimidazole and "x" indicates the molar ratio of Zn in the initial bi-MOF). As illustrated in Figure 1, no other post-treatments were involved (see Experimental for details). The presence of Zn species not only form a spatial isolation for Co to suppress its sintering, but also increase the specific surface area of the resulting catalysts due to the evaporation of Zn during pyrolysis. Fine tuning of the original Zn content allowed us to optimize its specific surface area, porosity, Co nanoparticle size, and hence ORR activity. Electrocatalytic studies showed that the carbonization of $Zn_{0.8}Co_{0.2}(MeIM)_2$ resulted in the most active Co-N-C for ORR. Therefore, unless noted otherwise, Co-N-C discussed hereafter was derived from $Zn_{0.8}Co_{0.2}(MeIM)_2$ frameworks. The optimal Co-N-C showed very high ORR activity with a half-wave potential of 0.871 V vs RHE (30 mV more positive than that of commercial 20 wt% Pt/C, 0.841 V vs RHE), and a kinetic current density of 39.3 mA cm^{-2} at 0.80 V (3.1 times that of Pt/C, 12.4 mA cm^{-2}) in 0.1 M KOH, superior to those of most reported nonprecious ORR catalysts as well (Table S1). Moreover, Co-N-C also exhibited excellent ORR activity and stability in acidic and neutral electrolytes. Various characterization techniques including X-ray absorption spectroscopy revealed that the superior activity and strong stability of Co-N-C originated from the intense interaction between Co and N, high content of ORR active pyridinic and pyrrolic N, along with large specific surface area. We believe this bi-MOF self-adjusted synthetic strategy can be extended to produce other M-N-C catalysts for multiple energy-related applications

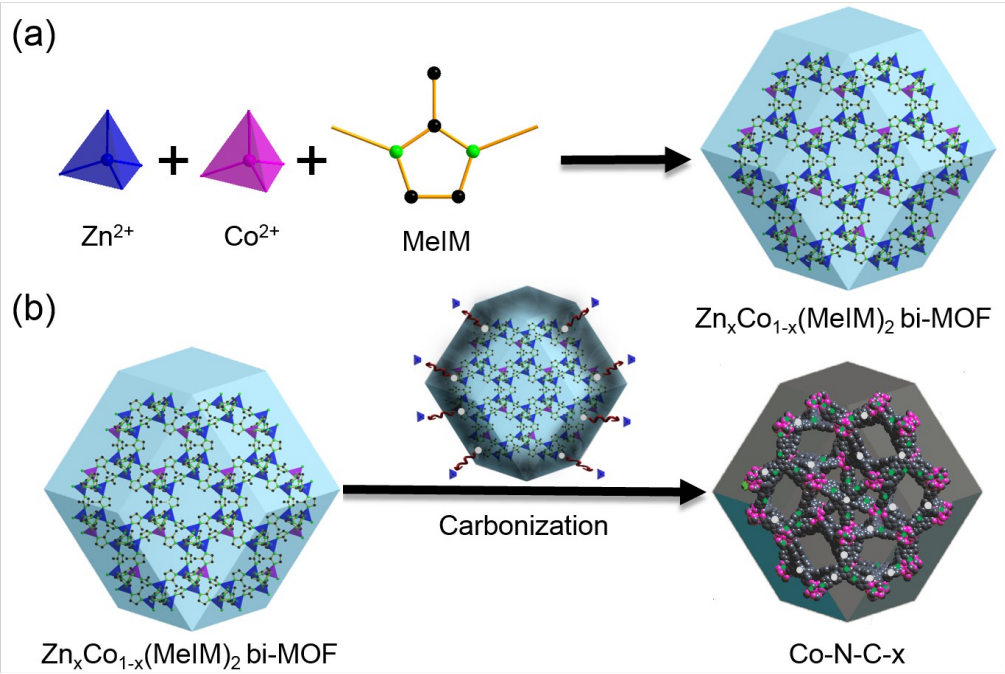

Figure 1. Illustration of bi-MOF self-adjusted synthesis of Co-N-C-x. (a) Formation of Zn/Co bi-MOF, $Zn_xCo_{1-x}(MeIM)_2$. (b) Carbonization of the Zn/Co bi-MOF to produce Co-N-C-x without any additional procedures and during carbonization Zn evaporation occurs.

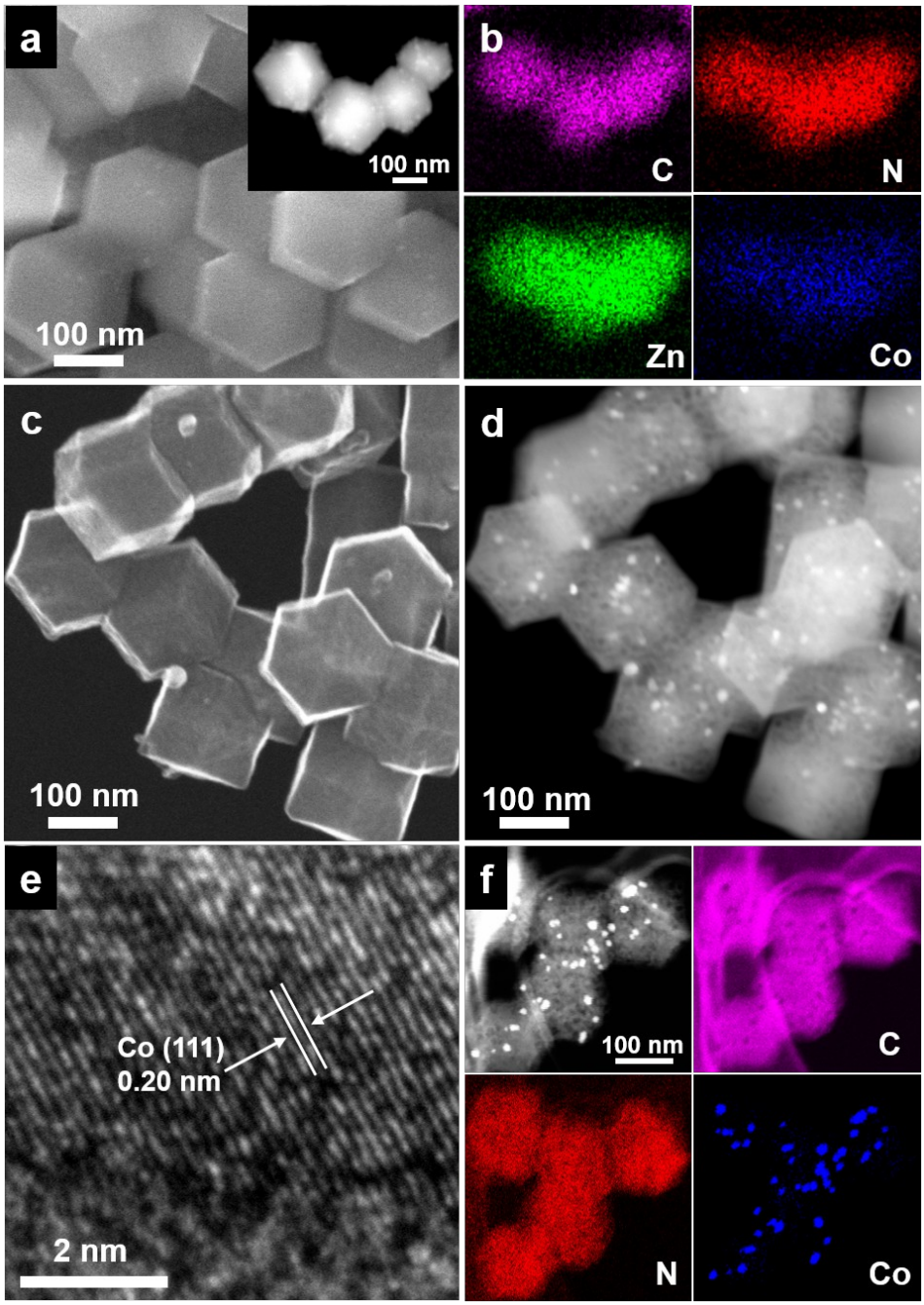

Figure 2. Physical characterizations. (a) SEM and STEM (inset) images of $Zn_{0.8}Co_{0.2}(MeIM)_2$ bi-MOF. (b) The corresponding element mapping images of (a) inset. (c) SEM and (d) STEM images of Co-N-C derived from $Zn_{0.8}Co_{0.2}(MeIM)_2$ bi-MOF. (e) HR-TEM image of Co-N-C. (f) STEM and the element mapping images of Co-N-C.

RESULTS AND DISCUSSION

As revealed by scanning electron microscopy (SEM) and scanning transmission electron microscopy (STEM), uniform polyhedron-like bi-MOF named as $Zn_{0.8}Co_{0.2}(MeIM)_2$ could be obtained (Figure 2a and Figure S1a-b). Element mapping analysis suggested the well-proportioned distribution of Zn, Co, C and N (Figure 2b). It is clear that the uniformly dispersed Zn species spatially isolated the Co species and diluted the Co concentration. Energy-dispersive X-ray spectroscopic (EDX) analysis corroborated the molar ratio of Zn and Co close to 4 (Figure S2a). The X-ray diffraction (XRD) patterns of all the $Zn_xCo_{1-x}(MeIM)_2$ samples (x = 0~1) confirmed their high crystallinity and similar zeolite-type structure (Figure S3a).[41] Upon carbonization, the resulting Co-N-C inherited the overall polyhedron-like morphology of the parent $Zn_{0.8}Co_{0.2}(MeIM)_2$ (Figure 2c and Figure S1c,d). Remarkably, the corresponding STEM images revealed that Co-N-C consisted of fine Co nanoparticles with a mean diameter of ~9.5 nm sparsely and uniformly embedded in the porous carbon matrices (Figures 2d and S1e). In sharp contrast, the control samples with lower Zn contents resulted in severe Co aggregation (Figure S4). These results clearly demonstrate that the presence of Zn species at high content could effectively suppress Co sintering during carbonization due to a spatial isolation of Co by Zn species. High resolution TEM (HR-TEM) images revealed a lattice fringe of 0.20 nm for an embedded Co nanoparticle (Figure 2e), corresponding to the (111) plane of face-centered cubic metallic Co (PDF: 15-0806). High-angle annular dark-field STEM (HAADF-STEM) and the corresponded element mapping (Figure 2f) confirmed the uniform distribution of C, N, and highly dispersed Co nanoparticles. The presence of metallic Co in Co-N-C was also confirmed by its XRD pattern (Figure S3b). EDX analysis (Figure S2b) exhibited the presence of Co, N, and C, and the absence of Zn. We anticipated the evaporation of Zn during carbonization would substantially improve the specific surface area of the final Co-N-C. Indeed, the measured specific surface area (Figure S5) of Co-N-C-x is highly correlated with the starting Zn/Co molar ratio. When the starting Zn content increased from 0, 50%, 67%, 80%, to 89% and 100%, the resulting Co-N-C-x possessed increasing surface area from 206, 227, 328, 484, to 574 and 687 $m^2\ g^{-1}$ respectively. This trend undoubtedly demonstrated that the bi-MOF, $Zn_xCo_{1-x}(MeIM)_2$, with different percentages of Zn could not only modulate the Co nanoparticle size (suppressing sintering), but also regulate the specific surface area of the final Co-N-C, without any additional processes such as longstanding acid

leaching and/or iterative high temperature annealing (Tables S1 and S2). To the best of our knowledge, this “self-adjusted” route in bi-MOF has rarely been reported for ORR electrocatalysis. X-ray photoelectron spectroscopy (XPS) showed that Co-N-C mainly consisted of C, Co, and N (Figure S6a), consistent with the element mapping and EDX results. High-resolution Co 2p spectrum (Figure S6b) further confirmed the presence of metallic Co.[24] High-resolution N 1s spectrum (Figure S6c) can be fitted by three sub-peaks corresponding to pyridinic N (398.7 eV, 47%), pyrrolic N (400.5 eV, 43%), and oxidized N (403.7 eV, 10%).[24−34] The contents of Co and N measured by inductively coupled plasma-atomic emission spectrometry and element analysis were 10.6 wt% and 8.5 wt%, respectively. It’s anticipated that the well-dispersed Co nanoparticles with small size in the porous carbon skeleton and high N content with large percentages (90%) of pyridinic (47%) and pyrrolic (43%) N can reduce the energy barrier of O_2 adsorption and accelerate the rate-limiting first electron transfer step of ORR;[21] simultaneously the large surface area of Co-N-C will promote the accessibility of active sites,[11] thus synergistically resulting in superior electrocatalytic ORR activity.

The electrocatalytic ORR performance of Co-N-C was first studied by steady-state linear sweep voltammetry (LSV) on a rotating disk electrode (RDE) in O_2-saturated 0.1 M KOH. As shown in Figure S7, the best ORR activity was achieved at Zn molar content of 0.8 and carbonization temperature of 900 ^{o}C (denoted as Co-N-C for brevity), as judged by the onset (E_{onset}) and half-wave ($E_{1/2}$) potentials of the RDE polarization curves.[14−21] Our Co-N-C exhibited significantly higher activity than those of carbonized ZIF-8 (precursor $Zn(MeIM)_2$, no Co) and carbonized ZIF-67 (precursor $Co(MeIM)_2$, no Zn) in terms of E_{onset} and $E_{1/2}$ (Figures 3a and c). More importantly, the E_{onset} of Co-N-C was almost the same as that of 20 wt % Pt/C (0.982 V vs RHE); while the $E_{1/2}$ of Co-N-C (0.871 V vs RHE) was more positive than those of Pt/C (0.841 V) and other reported nonprecious electrocatalysts, such as Ag-Co alloy (0.80 V vs RHE),[10] CNT/Fe_3C (0.861 V vs RHE)[26] and CPM-99Co/C (0.802 V vs RHE),[40] indicating the much higher electrocatalytic ORR activity of our Co-N-C. Additionally, the specific mass activity of Co-N-C at 0.80 V was calculated to be 18.9 A g^{-1}, also higher than those of Fe-NT-G (< 15 A g^{-1})[27] and CPM-99Co/C (< 15 A g^{-1}).[40] The Koutecky-Levich (K-L) plots from RDE polarization curves at different rotating speeds for Co-N-C (Figure 3b) between 0.82 and 0.20 V resulted in nearly parallel fitting lines and the calculated electron transfer number (n) was from 3.84 to 4.00, suggesting a four-electron ORR pathway.[2] Furthermore, the kinetic current density (J_k) derived from the intercept of K-L plots (Figure 3c and Figure S8) was

39.3 mA cm^{-2} at 0.80 V, substantially higher than those of carbonized ZIF-8 (~ 0 mA cm^{-2}), carbonized ZIF-67 (5.8 mA cm^{-2}), Pt/C (12.4 mA cm^{-2}), and most reported nonprecious catalysts such as CNT/HDC-1000 (8.3 mA cm^{-2})[17] and Fe-N_x/C (10.3 mA cm^{-2}).[30] The rotating ring disk electrode(RRDE) tests (Figure S8c) also showed a high electron transfer number above 3.84 (consistent with the K-L results) and a low H_2O_2 yield below 7.0 % for Co-N-C, both of which were superior to those of carbonized ZIF-67 and close to those of Pt/C (Figure 3d). In addition, Co-N-C exhibited excellent methanol tolerance (Figure 3e) and great stability (Figure 3f), as confirmed by their negligible variation of chronoamperometric curve after the introduction of 2 M methanol and a negative shift of only 5 mV for $E_{1/2}$ after 5000 continuous potential cycles, respectively. The SEM and STEM images of Co-N-C after 5000 continuous potential cycles still maintained the overall polyhedron-like morphology with well-dispersed Co nanoparticles, implying their superior stability (Figure S9a and b). The slight negative-shift of $E_{1/2}$ is likely due to the modest oxidation of metallic Co that exposed in O_2 environments during stability test, as revealed by the XPS analysis on post-catalysis Co-N-C (Figure S9c-e). In sharp contrast, an immediate response in chronoamperometric curve (Figure 3e) and a 25 mV loss of $E_{1/2}$ for Pt/C under the same conditions (Figure S8d) were observed. These results unambiguously demonstrate that our Co-N-C possess much better methanol tolerance and stronger durability than Pt/C. A more detailed comparison on various ORR catalytic parameters in 0.1 M KOH, such as $E_{1/2}$, J_k, and specific mass activity of Co-N-C and other reported ORR catalysts is included in Table S1.

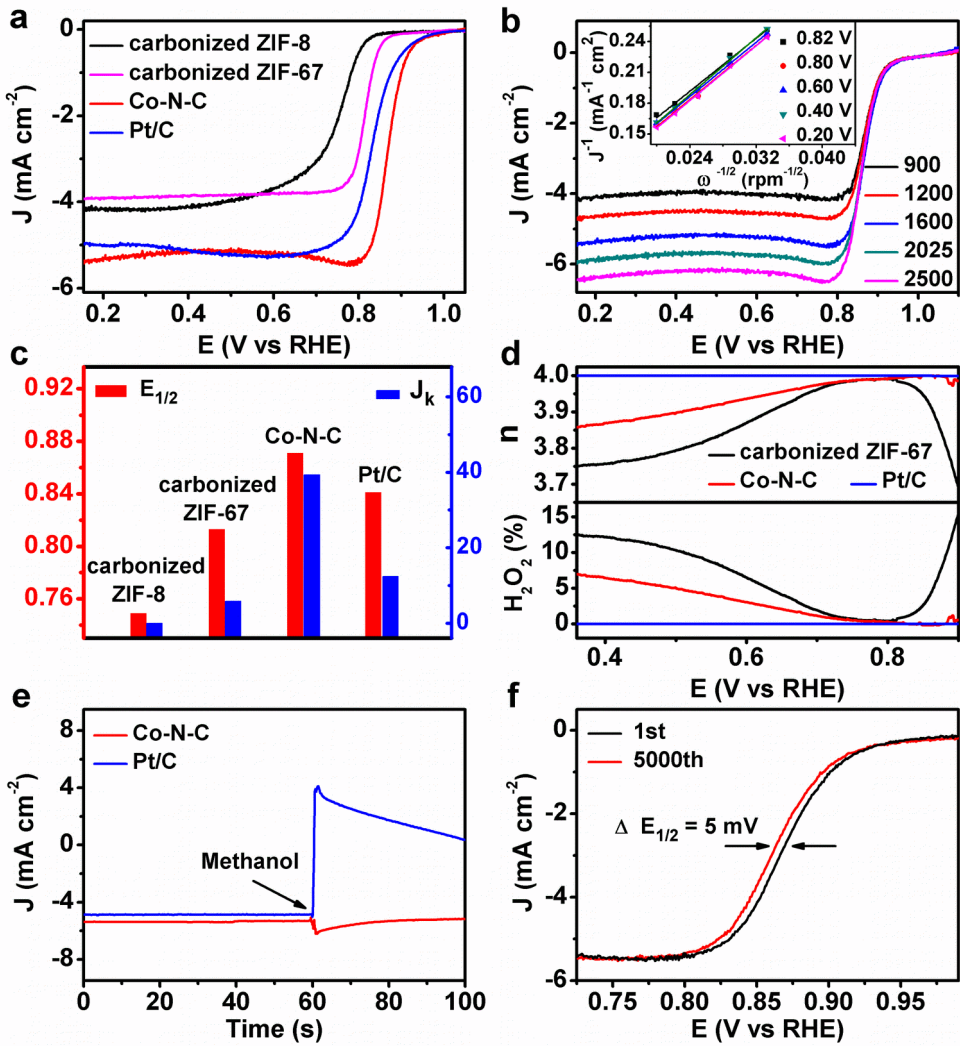

Figure 3. Electrocatalytic ORR results in O_2-saturated 0.1 M KOH. (a) RDE polarization curves of carbonized ZIF-8, carbonized ZIF-67, Co-N-C, and Pt/C at 10 mV s^{-1} and 1600 rpm. (b) RDE polarization curves of Co-N-C at different rotating speeds. Inset: K-L plots at different potentials. (c) Comparison of $E_{1/2}$ and J_k for different catalysts. (d) Electron transfer number (n) (top) and H_2O_2 yield (bottom) versus potential. (e) Chronoamperometric response of Co-N-C and Pt/C upon the addition of 2.0 M methanol at 0.70 V vs RHE. (f) RDE polarization curves of Co-N-C (near mixed-diffusion kinetic region) before and after 5000 potential cycles ranging from 1.15 to 0.15 V vs RHE.

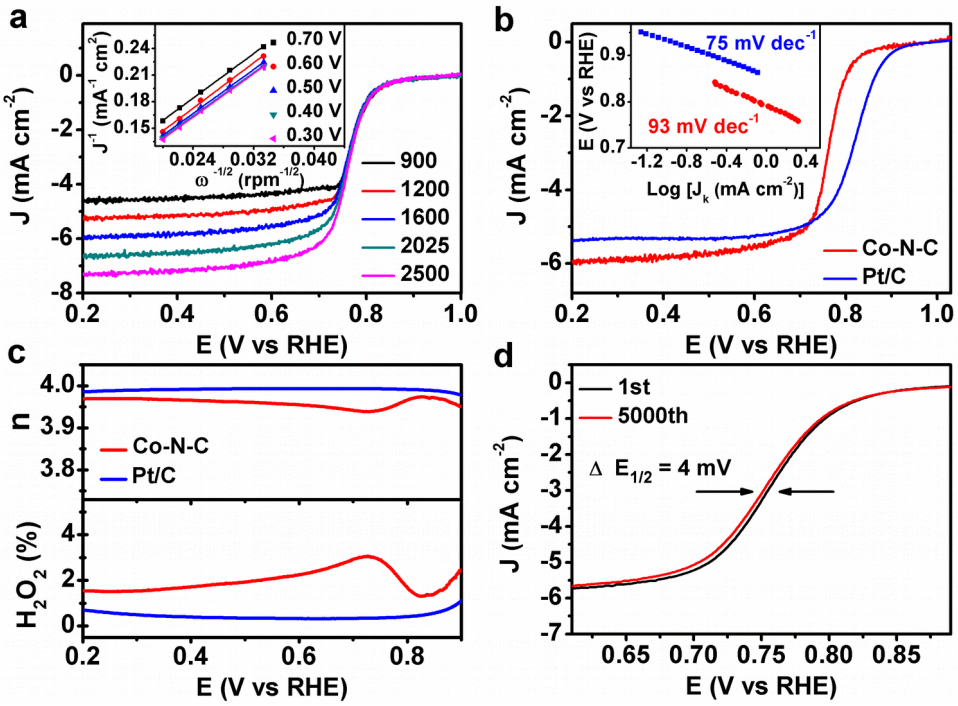

Figure 4. Electrocatalytic ORR results in O_2-saturated 0.1 M $HClO_4$. (a) RDE polarization curves of Co-N-C at 10 mV s^{-1} and different rotating speeds. Inset: K-L plots at different potentials. (b) RDE polarization curves of Co-N-C and Pt/C at 10 mV s^{-1} and 1600 rpm. Inset shows the corresponding Tafel plots. (c) Electron transfer number (n) (top) and H_2O_2 yield (bottom) of Co-N-C and Pt/C versus potential. (d) RDE polarization curves of Co-N-C (near mixed-diffusion kinetic region) before and after 5000 potential cycles ranging from 1.15 to 0.15 V vs RHE.

The remarkable ORR activity of Co-N-C under alkaline conditions prompted us to investigate their performance in acidic and neutral media. In 0.1 M $HClO_4$, all the RDE polarization curves of Co-N-C at different rotating speeds exhibited well-defined diffusion-limiting currents after a mixed kinetic-diffusion region (Figure 4a). Moreover, linearity of K-L plots and the near parallelism of the fitting lines suggested first-order reaction kinetics with respect to dissolved O_2 and a potential-independent electron transfer number (n) (Figure 4a inset).[2] The calculated n was 3.94~3.98, suggesting a four-electron ORR process, similar to those of Pt/C (Figures S10a and b). It was found that the $E_{1/2}$ of Co-N-C (0.761 V, Figure 4b) was only 59 mV lower than that of Pt/C (0.820 V) and much higher than those of reported nonprecious electrocatalysts such as meso/micro-PoPD (~0.70 V)[18] and PpPD-Fe-C (0.718 V).[33] The excellent ORR activity of Co-N-C was also gleaned from the small Tafel slope of 93 mV dec^{-1} at low overpotentials (close to the 75 mV dec^{-1} of Pt/C) and the high limiting current density of 6.02 mA cm^{-2} (Figure 4b), which was close to the theoretical value determined by the K-L equation and higher than those of Pt/C (5.38 mA cm^{-2}) and many other

nonprecious catalysts. Table S2 compares the ORR catalytic performance of Co-N-C and other reported catalysts in strong acidic electrolyte, clearly demonstrating the superior ORR activity of our Co-N-C. The low H_2O_2 yield (< 3.1%) and high n (>3.94) of Co-N-C obtained by RRDE measurements (Figure 4c) also verified this conclusion. Furthermore, Co-N-C showed much better stability than Pt/C, as revealed by a much smaller negative shift of $E_{1/2}$ (4 mV vs. 29 mV) after 5000 continuous potential cycles (Figure 4d and Figure S10c).

In neutral phosphate buffer, the RDE polarization curves of Co-N-C at different rotating speeds also exhibited well-defined diffusion-limiting currents after a mixed kinetic-diffusion region, good linearity of K-L plots and the nice parallelism of the fitting lines (Figure 5a), similar to those of Pt/C (Figure S11a and b). Furthermore, Co-N-C showed a relatively positive $E_{1/2}$ of 0.731 V, a high limiting current density of 6.01 mA cm^{-2}, and a small Tafel slop of 97 mV dec^{-1} (Figure 5b). All of them are close to those of Pt/C (0.768V, 6.02 mA cm^{-2}, and 97 mV dec^{-1}), implying a comparable ORR activity. Notably, the specific mass activity of Co-N-C at 0.20 V vs RHE was 10.0 A g^{-1}, significantly higher than those of previously reported nonprecious catalysts such as CoFe-PDAP (4.9 A g^{-1}).[24] The RRDE study revealed a low H_2O_2 yield (< 16%) and a high n (> 3.67). These values were close to those of Pt/C (H_2O_2 yield of < 4.5% and n > 3.87), indicating a high selectivity of Co-N-C towards the four-electron reduction of O_2 (Figure 5c). A negative $E_{1/2}$ shift of only 7 mV was observed for Co-N-C after 5000 continuous potential cycles (Figures 5d), while there was 25 mV $E_{1/2}$ loss for Pt/C under the same condition (Figure S11c), suggesting a better durability of Co-N-C than that of Pt/C.

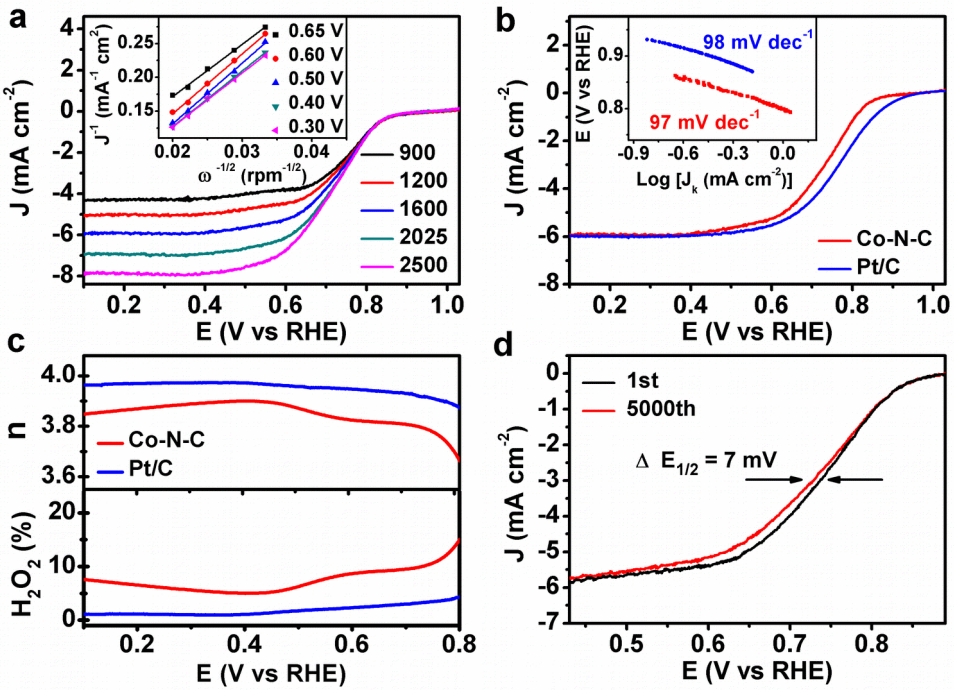

Figure 5. Electrocatalytic ORR results in O_2-saturated 0.1 M neutral phosphate buffer. (a) RDE polarization curves of Co-N-C at 10 mV s^{-1} and different rotating speeds. Inset: K-L plots at different potentials. (b) RDE polarization curves of Co-N-C and Pt/C at 10 mV s^{-1} and 1600 rpm. Inset shows the corresponding Tafel plots. (c) Electron transfer number (n) (top) and H_2O_2 yield (bottom) of Co-N-C and Pt/C versus potential. (d) RDE polarization curves of Co-N-C (near mixed-diffusion kinetic region) before and after 5000 potential cycles ranging from 1.15 to 0.15 V vs RHE.

To gain deeper insights about the superior ORR activity of Co-N-C, the X-ray absorption near-edge structure (XANES) spectra of Co-N-C, carbonized ZIF-8 and carbonized ZIF-67 were collected (Figure 6 and Figure S12). The drastic difference in the Co K-edge of the Co-N-C compared to cobalt oxides (CoO and Co_3O_4) unambiguously excludes the major involvement of the latter in our Co-N-C (Figure 6a and Figure S12a). In fact, the Co K-edge of carbonized ZIF-67 is very similar to that of Co foil, indicating the metallic Co nature of those large Co particles. However, the Co K-edge of Co-N-C was shifted to higher energy relative to that of carbonized ZIF-67, implying a much stronger interaction between Co and coordinated N, which would cause more electron transfer from Co to N.[47] Such a positive shift in energy was also observed in the Co L-edge of the two samples (Figure S12b). Similar to Fe-N-C catalysts, the electron-withdrawing character of N leads to lower electron density at the Co center and hence anodic shift in its redox potential (a downshift of the Co e_g orbital),[30] which will optimize the bond strength between Co and ORR intermediates and subsequently result in higher ORR activity. Such a Co-N interaction would also lead to a negative

shift of the pyridinic π* transitions in the N K-edge, as verified by the results in Figure 5b. It was also found that the total content of ORR active pyridinic and pyrrolic N (7.65 wt%) [48] in Co-N-C was much higher than those of carbonized ZIF-8 (6.73 wt%) and ZIF-67 (<1.1 wt%), which further promoted ORR activity (Table S3). In addition, Zn evaporation during pyrolysis can also boost the specific surface area of Co-N-C (484 $m^2 g^{-1}$) compared to that of carbonized ZIF-67 (206 $m^2 g^{-1}$), thus promoting the accessibility of ORR active sites and mass transport. Collectively, the small Co nanoparticle size, intense interaction between Co and N, high content of ORR active pyridinic and pyrrolic N as well as large specific surface area synergistically render Co-N-C outstanding ORR activity. It should be noted that in the N K-edge (Figure 6b), the peak at ~389 eV and the shoulder at ~397.5 eV are due to the 2nd harmonic Co L_3- and L_2-edge signals (Figure S12b). The higher intensities of these features in carbonized ZIF-67 than those of Co-N-C are consistent with the higher Co content in the former.

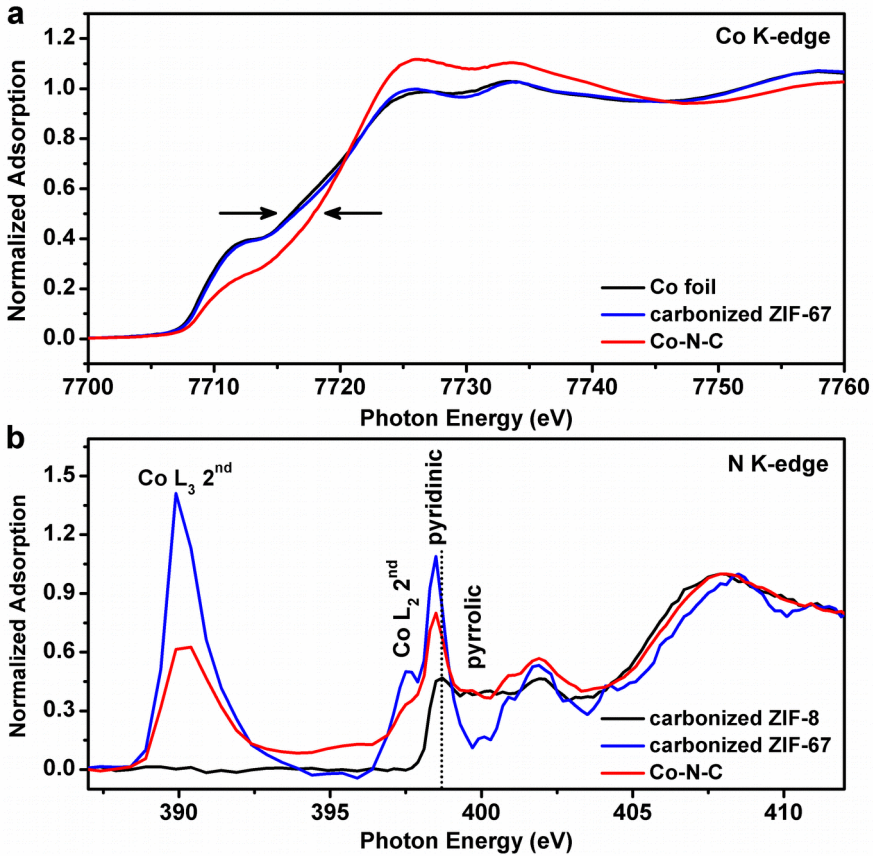

Figure 6. XAS characterization. (a) Co K-edge XANES spectra of Co foil, carbonized ZIF-67 and Co-N-C. (b) N K-edge XANES spectra of carbonized ZIF-8, carbonized ZIF-67 and Co-N-C.

It should be noted that Jiang et al. reported ZIF-8 and ZIF-67 derived ORR catalysts during the submission of our work.[49] A thorough investigation into their work and comparison with the results

described herein reveal several apparent advantages of our catalysts. First, similar to most reported metal-nitrogen-carbon-based ORR catalysts which require tedious post-treatments like strong acid etching and multiple annealing (see Tables S1 and S2 for more details), the catalysts reported by Jiang et al. required these laborious post-treatments (strong acid leaching and high temperature annealing). In addition, a second high temperature annealing with toxic phosphorous source (triphenylphosphine) was required to achieve the final P-doped catalyst to further boost the ORR activity. In contrast, our synthetic procedure is very facile and straight forward. After carbonization once, the resulting materials can be directly used as ORR electrocatalysts without any post-treatments and/or additives. To the best of our knowledge, such a simple procedure to achieve high-quality ORR catalysts has rarely been reported. Secondly, our Co-N-C catalyst exhibited superior ORR activity in 0.1 M KOH with $E_{1/2}$ of 0.871 V vs. RHE, which is much better than those reported by Jiang and many others (see Table S1). Furthermore, our Co-N-C also demonstrated remarkable ORR performance in acidic (see Figure 4 and Table S2) and neutral electrolytes (Figure 5). Finally, synchrotron X-ray absorption spectroscopy, coupled with detailed XPS and elemental analysis data allowed us to obtain more insights into the origin of the composition-structure-activity relationship, which were lack in Jiang's report. In fact, because of the phosphidation step, the composition of their optimal catalyst is already different from that of our Co-N-C.

CONCLUSION

In summary, we have described a facile and novel bi-MOF self-adjusted strategy to synthesize self-supported porous Co-N-C nanopolyhedron electrocatalysts by direct pyrolysis of Zn and Co bimetal-organic frameworks without any post-treatments such as longstanding acid leaching and/or iterative high temperature annealing. The optimal Co-N-C exhibit three dimensional hierarchical porosity, high specific surface area (484 $m^2 g^{-1}$), well-dispersed Co nanoparticles (~9.5 nm), and high N content (8.5%). With such a tailored composition and architecture as well as intense interaction between Co and N, the Co-N-C exhibited excellent ORR activity with $E_{1/2}$ of 0.871 V vs RHE and J_k of 39.3 mA cm^{-2} at 0.80 V in 0.1 M KOH, which are better than those of commercial 20 wt% Pt/C ($E_{1/2}$ of 0.841 V and J_k of 12.4 mA cm^{-2}) and most reported nonprecious electrocatalysts. Additionally, our Co-N-C also showed comparable ORR activity and much better stability than Pt/C even in acidic

and neutral electrolytes. Overall, the simplicity and low cost of the bi-MOF self-adjusted method endows it with a high promise for large-scale catalyst preparation. Moreover, such a strategy should be extendable to prepare other transition metal-nitrogen-carbon composites for various energy-related applications.

EXPERIMENTAL SECTION

Synthesis of Co-N-C catalysts. All chemicals were used as received without any further purification. In a typical preparation, 12 mmol transition metal nitrate ($Co(NO_3)_2·6H_2O$ or $Zn(NO_3)_2·6H_2O$ or their mixture with different Zn molar contents) were dissolved in 120 mL methanol to form a clear solution, which was subsequently poured into 40 mL methanol containing 48 mmol 2-methylimidazole (MeIM). After thorough mixing and incubation at room temperature, the as-obtained precipitates were centrifuged and washed with ethanol several times, resulting in $Zn_xCo_{1-x}(MeIM)_2$ bi-MOF, wherein "x" (x = 0~1) represents the molar content of Zn ions in the reactants. The powder of $Zn_xCo_{1-x}(MeIM)_2$ was placed in a tube furnace and then heated to the desired temperature (800, 900 and 1000 °C) for 3h under Ar to obtain the self-supported Co-N-C-x-y, wherein "x" represents the molar content of Zn ions in the initial bi-MOF precursor and "y" represents the carbonization temperature. The as-prepared Co-N-C-x-y were directly used as ORR electrocatalysts without any post-treatments. A series of samples including Co-N-C-0.8-800, Co-N-C-0.8-900 (denoted as Co-N-C for brevity in the main text), Co-N-C-0.8-1000, Co-N-C-0-900 (carbonized ZIF-67), Co-N-C-0.5-900, Co-N-C-0.67-900, Co-N-C-0.89-900, and N-C-900 (carbonized ZIF-8) could be obtained by using the appropriate molar content of Zn ions in the reactants and the pyrolysis temperature.

Characterizations. Scanning electron microscopy (SEM) and scanning transmission electron microscopy (STEM) measurements were collected on a FEI QUANTA FEG 650 (FEI, USA). High-angle annular dark-field scanning transmission electron microscopy (HAADF-STEM) and element mapping were collected on a JEM-2800 scanning transmission electron microscope (JEOL, Japan). TEM and STEM imaging were collected at 80 kV beam energy to minimize knock-off damage on the graphite structures and probe size used for STEM imaging was 1.0 nm. X-ray diffraction (XRD) patterns were recorded on a Rigaku MinifexII Desktop X-ray diffractometer. Nitrogen sorption isotherms were measured at 77 K with an autosorb iQ automated gas sorption analyzer (Quantachrome Instruments, USA). Before measurements, the samples were degassed under vacuum at 200 °C for 6 h. The Brunauer-Emmett-Teller (BET) method was utilized to calculate the specific surface area. The cobalt and nitrogen contents were analyzed by a Thermo Electron

iCAP inductively coupled plasma atomic emission spectrophotometer (ICP-AES) and an inductively coupled plasma-mass spectrometer (ICP-MS), respectively. The X-ray photoelectron spectroscopy analyses were performed using a Kratos Axis Ultra instrument (Chestnut Ridge, NY) at the Surface Analysis Laboratory, University of Utah Nanofab. The samples were affixed on a stainless steel Kratos sample bar, loaded into the instrument's load lock chamber, and evacuated to 5×10^{-8} torr before it was transferred into the sample analysis chamber under ultrahigh vacuum conditions (~10^{-10} torr). X-ray photoelectron spectra were collected using the monochromatic Al Kα source (1486.7 eV) at a 300 × 700 μm spot size. Low resolution survey and high resolution region scans at the binding energy of interest were collected for each sample. To minimize charging, all samples were flooded with low-energy electrons and ions from the instrument's built-in charge neutralizer. The samples were also sputter cleaned inside the analysis chamber with 1 keV Ar^+ ions for 30 seconds to remove adventitious contaminants and surface oxides. XPS data were analyzed using CASA XPS software, and energy corrections on high resolution scans were calibrated by referencing the C 1s peak of adventitious carbon to 284.5 eV.

The cobalt K-edge spectra were collected at the Advanced Light Source (ALS) at Lawrence Berkeley National Laboratory on beamline 10.3.2 with an electron energy of 1.9 GeV and an average current of 500 mA. The radiation was monochromatized by a Si (111) double-crystal monochromator. Intensity of the incident X-ray was monitored by an N_2-filled ion chamber (I_0) in front of the sample. Fluorescence spectra were recorded using a seven-element Ge solid-state detector. The monochromator energy was calibrated with Co foil rising edge energy (7709.5 eV). Data reduction of the XAS spectra was performed using custom-made software (Dr. Matthew Marcus). Pre-edge and post-edge contributions were subtracted from the XAS spectra, and the results were normalized with respect to the edge jump. The other X-ray absorption spectra were collected at bending magnet beamline 6.3.1 (1011 photons/s). Powder samples were pressed into In foil before mounting to a Cu sample plate. The energy of the incident X-ray beam was controlled with a variable line spacing plane grating monochromator (VLS-PGM) and its intensity monitored with a gold mesh upstream of the samples. All spectra were collected in total electron yield (TEY) mode. For the N K-edge spectra, the baselines were fit to third-order polynomials and removed, and spectral intensities were normalized to the peak near 408 eV. The nitrogen K-edge spectrum of polycrystalline h-BN powder was collected in TEY mode and used for energy calibration of all N K-edge spectra. Co L-edge spectra were subjected to a linear baseline correction, and spectral intensities were normalized to the post-edge intensity at 810.9 eV. The Co L-edge spectrum of Co_3O_4 powder was collected in TEY mode and used for energy calibration of all Co L-edge

spectra.

Electrocatalytic measurements. The nonprecious catalysts and commercial 20 wt% Pt/C samples were prepared by ultrasonically mixing 4 mg of the catalyst powder with the mixture of 1160 μL ethanol, 800 μL H_2O and 40 μL 5 % Nafion solution for 20 min to form homogeneous catalyst inks. Next, a certain volume of the catalyst ink was carefully dropped onto the polished glassy carbon rotating disk electrode (RDE) or rotating ring disk electrode (RRDE), leading to a desirable catalyst loading. In the basic electrolyte (0.1 M KOH), the nonprecious catalyst loading was 0.283 mg cm^{-2}; while in acidic electrolyte (0.1 $HClO_4$) and neutral phosphate buffer, the loading of nonprecious catalysts was 0.6 mg cm^{-2}. The loading of commercial 20 wt %Pt/C (Premetek Co.) was in all the three electrolytes was 0.142 mg cm^{-2}. Electrochemical measurements of linear sweep voltammetry (LSV) on the rotating disk electrode (RDE) were performed by a computer-controlled Gamry Interface 1000 electrochemical workstation and a RRDE-3A apparatus with a three-electrode cell system. A glassy carbon RDE (d = 3 mm, S = 0.07065 cm^2) coated with the catalyst ink was used as the working electrode, an Ag/AgCl (sat. KCl) electrode as the reference electrode, and a Pt wire as the counter electrode. All potentials reported in our work were quoted with respect to reversible hydrogen electrode (RHE). The calibration was performed in the high-purity hydrogen saturated electrolyte with a Pt wire as the working electrode. Cyclic voltammetry (CV) was run at a scan rate of 1 mV s^{-1}, and the average of the two potentials at which the current crossed zero was taken to be the thermodynamic potential for the hydrogen electrode reactions. The electrochemical experiments were conducted in O_2-saturated 0.1 M KOH, 0.1 M $HClO_4$, and 0.1 M neutral phosphate buffer for the oxygen reduction reaction at room temperature. The potential range was cyclically scanned at a scan rate of 10 mV s^{-1} at various rotating speed from 900 to 2500 rpm. The electron transfer number (n) and kinetic current density (J_k) were calculated from Koutecky-Levich equation, at various electrode potentials:

$$\frac{1}{J}=\frac{1}{J_L}+\frac{1}{J_K}=\frac{1}{B\omega^{\frac{1}{2}}}+\frac{1}{J_K}$$

$$B=0.2nFC_0D_0^{\frac{2}{3}}V^{\frac{-1}{6}}$$

where J is the measured current density, J_K and J_L are the kinetic and limiting current densities, ω is the rotating speed (rpm), n is the electron transfer number, F is the Faraday constant (96485 C mol^{-1}), C_0 is the bulk concentration of O_2 (1.2×10^{-6} mol cm^{-3}), D_0 is the diffusion coefficient of O_2, and V is the kinematic viscosity of the electrolyte (0.01 cm^2 s^{-1}). In order to eliminate the inference of double layer capacitance, the electrolyte was deaerated by bubbling with N_2, and then the voltammogram was evaluated in the deaerated

electrolyte. The oxygen reduction current was calculated as the difference between currents measured in the deaerated and O_2-saturated electrolytes. For RRDE tests, a computer-controlled CHI 660A electrochemical workstation was employed and the disk electrode was scanned catholically at a rate of 5 mV s^{-1} and the ring electrode potential was set to 1.2 V vs. RHE. The hydrogen peroxide yield (H_2O_2 %) and the electron transfer number (n) were determined by the following equations:

$$H_2O_2(\%) = 200 \times \frac{\frac{I_r}{N}}{I_d + \frac{I_r}{N}}$$

$$n = 4 \times \frac{I_d}{I_d + \frac{I_r}{N}}$$

where I_d is the disk current, I_r is the ring current, and N is the current collection efficiency of the Pt ring, which was determined to be 0.40 from the reduction of $K_3Fe[CN]_6$. Each measurement was repeated 3 times in order to avoid any incidental error. The accelerated stability tests of the nonprecious catalysts and Pt/C were performed in all the O_2-saturated electrolytes (0.1 M KOH, 0.1 M $HClO_4$, and 0.1 M neutral phosphate buffer) at room temperature by potential cycling ranging from 1.15 to 0.15 vs RHE for 5,000 cycles. At the end of cycling, the final catalyst-loaded working electrode was subjected to polarization measurement. In order to highlight the difference of half-wave potential for Co-N-C before and after 5,000 cycles, we show the polarization curves near the mixed-diffusion region in the main text. iR (current times internal resistance) compensation was applied in all the electrochemical experiments to account for the voltage drop between the reference and working electrodes using Gamary Framework™ Data Acquisition Software 6.11.

AUTHOR INFORMATION

Corresponding Author

*E-mail: yujie.sun@usu.edu.

Notes

The authors declare no competing financial interest.

Acknowledgment. This work was supported financially by Utah State University. Y.S. acknowledges the support from the Microscopy Core Facility at Utah State University for some of the SEM work. N.J. acknowledges the Governor's Energy Leadership Scholars Grant of the Utah Energy Research Triangle. XAS experiments

were supported by the Joint Center for Artificial Photosynthesis, a DOE Energy Innovation Hub, supported through the Office of Science of the U.S. Department of Energy under Award Number DE-SC0004993, and performed at the Advanced Light Source (BL 6.3.1 and 10.3.2), Berkeley, under Contract DE-AC02-05CH11231.

Supporting Information Available: Supplementary figures and tables. This material is available free of charge via the Internet at http://pubs.acs.org.

REFERENCES AND NOTES

1 Debe, M. K. *Nature* **2013**, *486*, 43-51.
2 Guo, S.; Zhang, S.; Sun, S. *Angew. Chem. Int. Ed.* **2013**, *52*, 8526-8544.
3 Liu, M.; Zhang, R.; Chen, W. *Chem. Rev*. **2014**, *114*, 5117-5160.
4 Yuan, S.; Shui, J. L.; Grabstanowicz, L.; Chen, C.; Commet, S.; Reprogle, B.; Xu, T.; Yu, L.; Liu, D. J. *Angew. Chem. Int. Ed.* **2013**, *52*, 8349-8353.
5 Jung, J. I.; Jeong, H. Y.; Lee, J. S.; Kim, M. G.; Cho, J. *Angew. Chem. Int. Ed.* **2014**, *53*, 4582-4586.
6 Ye, T. N.; Lv, L. B.; Li, X. H.; Xu, M.; Chen, J. S. *Angew. Chem. Int. Ed.* **2014**, *53*, 6905-6909.
7 Jaouen, F.; Proietti, E.; Lefèvre, M.; Chenitz, R.; Dodelet, J. P.; Wu, G.; Chung, H. T.; Johnston, C. M.; Zelenay, P. *Energy Environ*. *Sci*. **2011**, *4*, 114-130.
8 Lefèvre, M.; Proietti, E.; Jaouen, F.; Dodelet, J. P. *Science* **2009**, *324*, 71-74.
9 Wu, G.; More, K. L.; Johnston, C. M.; Zelenay, P. *Science* **2011**, *332*, 443-447.
10 Holewinski, A.; Idrobo, J. C.; Linic, S. *Nat. Chem.* **2014**, *6*, 828-834.
11 You, B.; Yin, P.; An, L. *Small* **2014**, *10*, 4352-4361.
12 Katsounaros, I.; Cherevko, S.; Zeradjanin, A. R.; Mayrhofer, K. J. J. *Angew. Chem. Int. Ed.* **2014**, *53*, 102-121.
13 Zhou, Y.; Lu, Q.; Zhuang, Z.; Hutchings, G. S.; Kattel, S.; Yan, Y.; Chen, J. G.; Xiao, J. Q.; Jiao, F. *Adv. Energy Mater.* **2015**, *5*, 1500149.
14 Gong, K.; Du, F.; Xia, Z.; Durstock, M.; Dai, L. *Science* **2009**, *323*, 760-764.
15 Wang, S.; Zhang, L.; Xia, Z.; Roy, A.; Chang, D. W.; Baek, J. B.; Dai, L. *Angew. Chem. Int. Ed.* **2012**, *51*, 4209-4212.
16 Wang , S.; Iyyamperumal, E.; Roy, A.; Xue, Y.; Yu, D. Dai, L. *Angew. Chem. Int. Ed.* **2011**, *50*, 11756-11760.
17 Sa, Y. J.; Park, C.; Jeong, H. Y.; Park, S. H.; Lee, Z.; Kim, K. T.; Park, G. G.; Joo, S. H. *Angew. Chem. Int. Ed.* **2014**, *53*, 4102-4106.
18 Liang, H. W.; Zhuang, X.; Brüller, S.; Feng, X.; Müllen, K. *Nat. Commun.* **2014**, *5*, 4973.
19 Cheon, J. Y.; Kim, J. H.; Kim, J. H.; Goddeti, K. C.; Park, J. Y.; Joo, S. H. *J. Am. Chem. Soc.* **2014**, *136*, 8875-8878.
20 Meng, Y.; Voiry, D.; Goswami, A.; Zou, X.; Huang, X.; Chhowalla, M.; Liu, Z.; Asefa, T. *J. Am. Chem. Soc.* **2014**, *136*, 13554-13557.
21 Ding, W.; Wei, Z.; Chen, S.; Qi, X.; Yang, T.; Hu, J.; Wang, D.; Wan, L. J.; Alvi, S. F.; Li, L. *Angew. Chem. Int. Ed.* **2013**, *52*, 11755-11759.
22 Xiang, Z.; Cao, D.; Huang, L.; Shui, J.; Wang, M.; Dai, L. *Adv*. *Mater*. **2014**, *26*, 3315-3320.
23 Jasinski, R. *Nature* **1964**, *201*, 1212-1213.
24 Zhao, Y.; Watanabe, K.; Hashimoto, K. *J. Am. Chem. Soc.* **2012**, *134*, 19528-19531.
25 Lin, L.; Zhu, Q.; Xu, A. W. *J. Am. Chem. Soc.* **2014**, *136*, 11027-11033.
26 Yang, W.; Liu, X.; Yue, X.; Jia, J.; Guo, S. *J. Am. Chem. Soc.* **2015**, *137*, 1436-1439.
27 Li, Y.; Zhou, W.; Wang, H.; Xie, L.; Liang, Y.; Wei, F.; Idrobo, J. C.; Pennycook, S. J.; Dai, H. *Nat. Nanotechnol*. **2012**, *7*, 394-400.
28 Sahraie, R. N.; Paraknowitsch, J. P.; Göbel, C.; Thomas, A.; Strasser, P. *J. Am. Chem. Soc.* **2014**, *136*, 14486-14497.
29 Choi, C. H.; Lim, H. K.; Chung, M. W.; Park, J. C.; Shin, H.; Kim, H.; Woo, S. I. *J. Am. Chem. Soc.* **2014**, *136*, 9070-9077.
30 Ramaswamy, N.; Tylus, U.; Jia, Q.; Mukerjee, S. *J. Am. Chem. Soc.* **2013**, *135*, 15443-15449.
31 Hu, Y.; Jensen, J. O.; Zhang, W.; Cleemann, L. N.; Xing, W.; Bjerrum, N, J.; Li, Q. *Angew. Chem. Int. Ed.* **2014**, *53*, 3675-3679.
32 Wen, Z.; Ci, S.; Hou, Y.; Chen, J. *Angew. Chem. Int. Ed.* **2014**, *53*, 6496-6500.
33 Zhu, Y.; Zhang, B.; Liu, X.; Wang, D. W.; Su, D. S. *Angew. Chem. Int. Ed.* **2014**, *53*, 10673-10677.
34 Wang, X.; Zhou, J.; Fu, H.; Li, W.; Fan, X.; Xin, G.; Zheng, J.; Li, X. *J. Mater. Chem. A* **2014**, *2*, 14064-14070.
35 Chung, H. T.; Won, J. H.; Zelenay, P. *Nat*. *Commun*. **2013**, *4*, 1922.
36 Strickland, K.; Miner, E.; Jia, Q.; Tylus, U.; Ramaswamy, N.; Liang, W.; Sougrati, M. T.; Jaouen, F.; Mukerjee, S. *Nat*. *Commun*. **2015**, *6*, 7343.
37 Sun, Y.; Liu, C.; Grauer, D. C.; Yano, J.; Long, J. R.; Yang, P.; Chang, C. J. *J*. *Am*. *Chem*. *Soc*. **2013**, *135*, 17699-17702.
38 Jiang, N.; You, B.; Sheng, M.; Sun, Y. *Angew*. *Chem*. *Int*. *Ed*. **2015**, *54*, 6251-6254.
39 Xia, W.; Mahmood, A.; Zou, R.; Xu, Q. *Energy Environ*. *Sci*. **2015**, *8*, 1837-1866.

40 Lin, Q.; Bu, X.; Kong, A.; Mao, C.; Zhao, X.; Bu, F.; Feng, P. *J. Am. Chem. Soc.* **2015**, *137*, 2235-2238.
41 Zhang, W.; Wu, Z. Y.; Jiang, H. L.; Yu, S. H. *J. Am. Chem. Soc.* **2014**, *136*, 14385-14388.
42 Aijaz, A.; Fujiwara, N.; Xu, Q. *J. Am. Chem. Soc.* **2014**, *136*, 6790-6793.
43 Ma, T. Y.; Dai, S., Jaroniec, M.; Qiao, S. Z. *J. Am. Chem. Soc.* **2014**, *136*, 13925-13931.
44 Zhong, H. X.; Wang, J.; Zhang, Y. W.; Xu, W. L.; Xing, W.; Xu, D.; Zhang, Y. F.; Zhang, X. B. *Angew. Chem. Int. Ed.* **2014**, *53*, 14235-14239.
45 Zhao, D.; Shui, J. L.; Grabstanowicz, L. R.; Chen, C.; Commet, S. M.; Xu, T.; Lu, J.; Liu, D. J. *Adv. Mater*. **2014**, *26*, 1093-1097.
46 Zhao, S.; Yin, H.; Du, L.; He, L.; Zhao, K.; Chang, L.; Yin, G.; Zhao, H.; Liu, S.; Tang, Z. *ACS Nano* **2014**, *8*, 12660-12668.
47 Kelly, D. N.; Schwartz, C. P.; Uejio, J. S.; Duffin, A. M.; England, A. H.; Saykally, R. J. *J. Chem. Phys.* **2010**, *133*, 101103-101106.
48 Leinweber, P.; Kruse, J.; Walley, F. L.; Gillespie, A.; Eckhardt, K. U.; Blyth, R.; Regier, T. *J. Synchrotron Rad.* **2007**, *14*, 500-511.
49 Chen, Y. Z.; Wang, C.; Wu, Z. Y.; Xiong, Y.; Xu, Q.; Yu, S. H.; Jiang, H. L. *Adv. Mater*. **2015**, *27*, 5010-5016.

Table of Contents